



Influence of textural parameters on the catalytic behavior for CO oxidation over ordered mesoporous Co_3O_4

Shijiao Sun, Qiuming Gao*, Huanlei Wang, Jingkang Zhu, Hongliang Guo

State Key Laboratory of High Performance Ceramics and Superfine Microstructures, Shanghai Institute of Ceramics, Graduate School, Chinese Academy of Sciences, 1295 Dingxi Road, Shanghai 200050, PR China

ARTICLE INFO

Article history:

Received 25 January 2010

Received in revised form 12 April 2010

Accepted 13 April 2010

Available online 18 April 2010

Keywords:

Nanocasting

KIT-6 silica

Mesoporous Co_3O_4

CO oxidation

ABSTRACT

Ordered mesoporous Co_3O_4 has been synthesized by nanocasting from three-dimensional cubic KIT-6 template. The cobalt precursor is introduced into the silica pores by the “bi-solvent” method. The structure and textural characteristics are investigated by X-ray diffraction, Fourier transform infrared spectroscopy, transmission electron microscopy, nitrogen sorption at 77 K. By changing the hydrothermal temperature of the KIT-6 template, two kinds of Co_3O_4 replicas with different mesostructured symmetries are obtained. Mesoporous Co_3O_4 oxides prepared from KIT-6 aged at low temperature have uncoupled sub-frameworks while mesoporous Co_3O_4 oxides prepared from KIT-6 aged at high temperature possess coupled sub-frameworks. CO oxidation is carried out as a model reaction to evaluate the catalytic activity. Co_3O_4 replicas with uncoupled sub-frameworks which possess higher surface area and more open pore system exhibit better performance than Co_3O_4 replicas with coupled sub-frameworks. The light-off temperature of CO oxidation reaches as low as 68 °C with a space velocity of 120,000 $\text{mL h}^{-1} \text{g}_{\text{cat}}^{-1}$ over the uncoupled Co_3O_4 replica. Calcination temperature of the cobalt precursor only has negligible or slight impact on the catalytic activity.

© 2010 Elsevier B.V. All rights reserved.

1. Introduction

The catalytic oxidation of carbon monoxide to carbon dioxide is of importance in many processes, such as automotive emission control, air purification, close-cycle CO_2 lasers and CO gas sensors [1–3]. Besides, with the development of polymer electrolyte fuel cell (PEFC), the produced hydrogen fuel is as a result of the steam reforming of hydrocarbons. However, the hydrogen fuel produced often contains a certain amount of CO, which is poisonous to the Pt anode and reduces the performance of the PEFC. Hence, preferential oxidation of CO in the H_2 -rich stream has become urgent in recent years [4–8].

Supported noble metals (Au, Pt and Pd) are well-known CO oxidation catalysts with high activity and stability. Especially supported Au catalysts used as CO oxidation have been long and extensively investigated from various aspects [9–13]. Haruta and Goodman have reviewed the early advance in the supported Au catalysts. They found that the catalytic properties of Au strongly depended on the particle size and shape, support effect and deposition methods [14,15]. Moreover, the high cost of precious metals and their sensitivity to sulfur poisoning may inhibit their large-

scale applications, which have motivated the search for substitute catalysts [16]. Transition metal oxide materials are of interest when they are designed as catalysts since they are less expensive relative to the precious metal catalysts [17]. The well-known example of the transition metal oxide catalyst for CO oxidation is Hopcalite, which is based on manganese–copper mixed oxide. Hopcalite has cost-competitiveness and has been widely used for the respiratory system [18–21]. Besides, a range of transition metal oxide catalysts (bulk or supported) have been reported for CO oxidation in the recent literatures including copper iron composite oxide catalysts [22,23], $\text{CuO/Ce}_{0.8}\text{Zr}_{0.2}\text{O}_2$ [24,25], MnO_x nanocrystal [26], copper-containing mesoporous manganese oxides [27], meso-/macroporous ZnO-CeO_2 [28] and CeO_2 with different morphologies [29,30].

Ordered mesoporous metal oxides are of wide interest for application in catalysis either as supports or catalysts themselves. There are mainly two routes to synthesize the ordered mesoporous metal oxides: soft chemical and hard-templating routes. In the hard-templating (nanocasting) pathway, pioneered by the group of Ryoo with the preparation of ordered mesoporous carbon (CMK-type family), suitable precursors are incorporated in the pores and channels of highly ordered mesoporous silicas. After solidification achieved within the pores, the parent silica materials can be selectively removed and shape-reversed molded structures can usually be obtained. The synthesis of mesoporous transition metal oxides

* Corresponding author. Tel.: +86 21 52412513; fax: +86 21 52413122.

E-mail address: qmgao@mail.sic.ac.cn (Q. Gao).

via the nanocasting pathway can deliver materials with highly ordered pore structures and highly crystalline walls, as well as good thermal stability compared to that by soft chemical templating route, which are beneficial for the catalytic performance [31]. A series of ordered mesoporous metal oxides prepared by nanocasting pathway used as highly efficient catalysts for CO oxidation have been investigated. For example, Shen et al. previously reported copper oxide-loaded mesoporous ceria catalysts for the CO oxidation [32]. In our group, Zhu et al. reported that mesoporous copper cerium bimetal oxides exhibited an excellent catalytic performance for the CO oxidation. The light-off temperature was as low as 350 K achieved over the catalyst with 20% copper contents [2]. Later, Zhu et al. also investigated a series of mesoporous spinels of MCo_2O_4 ($\text{M} = \text{Cu}, \text{Mn}$ and Ni) and found that CuCo_2O_4 and MnCo_2O_4 catalysts showed better activities and stabilities than NiCo_2O_4 . The lowest temperature of 50% CO conversion was 342 K over the copper cobalt oxide catalyst [33]. Very recently, Bruce and co-workers [31] systematically investigated a range of order mesoporous metal oxides with the same three-dimensional (3D) pore structure and found that mesoporous Co_3O_4 , $\beta\text{-MnO}_2$, and NiO showed an appreciable CO oxidation activity below 273 K.

On one hand, among a wide variety of transition metal oxides, spinel Co_3O_4 has become one of the most important functional materials due to its unique application in heterogeneous catalysis, anode material in Li-ion rechargeable battery, solid-state sensor, solar energy absorber, ceramic pigment, and electrochromic device [34]. On the other hand, to the best of our knowledge, there are few reports on nanocasting Co_3O_4 for CO catalytic oxidation so far. In addition, among the known mesostructures, the cubic structure with the space group $la3d$ is one of the most interesting structures. Its pore network topology can be represented as an interpenetrating bicontinuous network of channels. In contrast to materials with two-dimensional (2D) hexagonal symmetry, the 3D cubic pore structure is highly branched and accessible, making it an excellent template for the nanocasting approach [35]. In this paper we report the synthesis of ordered mesoporous Co_3O_4 using cubic $la3d$ mesoporous silica KIT-6 with different hydrothermal temperatures (40 and 130 °C) as the hard template. The cobalt nitrate hexahydrate was introduced into the silica pores by a “bi-solvent” method for the first time. The influences of hydrothermal temperature of the template on the structural and textual parameters of the Co_3O_4 replica and finally the CO catalytic activity were comprehensively investigated. Besides, the catalytic activities were compared between Co_3O_4 replica before and after dissolution of the silica template for the first time. Furthermore, we also studied the effect of calcination temperature of the precursor on the CO catalytic activity.

2. Experimental

2.1. Synthesis of mesoporous silica KIT-6

Cubic ordered mesoporous silica (KIT-6) was synthesized according to the literature with minor modification [36]. In a typical synthesis, 6 g of P123 was dissolved in 217 mL of distilled water with 11.8 g of conc. HCl (37%). 6 g of *n*-butanol was added to the mixture under stirring at 35 °C. Then, this mixture was stirred for 1 h at 35 °C before 12.9 g of TEOS was added. After stirring at 35 °C for another 24 h, the mixture was subsequently transferred into stainless-steel autoclaves which were sealed and maintained at two different temperatures, 40 or 130 °C for 24 h under static conditions. The resulting mixture was filtered without washing and dried at 80 °C. The organic template was removed by calcination at 550 °C for 6 h in air at a heating rate of 3 °C min⁻¹. The resulting mesoporous silica templates aged at 40 and 130 °C were denoted as KIT-6-40 and KIT-6-130, respectively.

2.2. Nanocasting of mesoporous Co_3O_4 catalysts

Synthesis of mesoporous Co_3O_4 was performed by the “bi-solvent” impregnation method reported previously by Davidson and co-workers [37]. Typically, 1.0 g of as-prepared KIT-6 was suspended in 40 mL of dry *n*-hexane. After stirring for 3 h at room temperature, 1 mL of 1.5 g/mL $\text{Co}(\text{NO}_3)_2 \cdot 6\text{H}_2\text{O}$ aqueous solution as the second solution was added dropwise under vigorous stirring. The mixture was stirred overnight. Then, a pink powder specimen was obtained by filtration and dried at room temperature. The solid was then calcined in a muffle furnace with a heating rate of 1 °C min⁻¹ from room temperature to 300 °C and maintained at this temperature for 5 h. The silica template was removed by etching twice with heated 2 M NaOH aqueous solution for 12 h each time. The template-free mesoporous Co_3O_4 was collected by filtering, washing with water and ethanol, and then dried at 80 °C. Mesoporous Co_3O_4 prepared by using KIT-6-40 and KIT-6-130 was denoted as Co_3O_4 -300-KIT-6-40 and Co_3O_4 -300-KIT-6-130, respectively. In addition, in order to investigate the influence of the calcination temperature of the precursor $\text{Co}(\text{NO}_3)_2 \cdot 6\text{H}_2\text{O}$ on catalytic activity, another two specimens designated as Co_3O_4 -500-KIT-6-40 and Co_3O_4 -500-KIT-6-130 were prepared following the same procedure described above except for the calcination temperature of 500 °C.

2.3. Material characterization

Powder X-ray diffraction (XRD) patterns were recorded on a Rigaku D/max 2200 X-ray diffractometer using Ni-filtered Cu K α radiation ($\lambda = 0.15418$ nm) operating at 40 kV and 40 mA. FTIR spectra were carried out on the Thermo Nicolet 7000-C Fourier Transform Spectrometer with ± 2 cm⁻¹ resolution between 4000 and 400 cm⁻¹ using KBr disk method. Transmission electron microscopy (TEM) images were measured on a JEOL JEM-2010 transmission electron microscope equipped with an Oxford energy-dispersive X-ray (EDX) spectrometer attachment operating at 200 kV. Nitrogen adsorption-desorption isotherms were measured on a Micromeritics ASAP 2020M analyzer at liquid nitrogen temperature (77 K). Prior to determination the isotherm, the samples were degassed at 423 K in vacuum for 5 h. The Brunauer–Emmett–Teller (BET) specific surface area was calculated using the adsorption data in the relative pressure (P/P_0) range from 0.05 to 0.3, and the total pore-volume was determined from the amount adsorbed at $P/P_0 = 0.98$. The pore-size distribution curve was calculated based on the desorption branch of the isotherm using the Barrett–Joyner–Halenda (BJH) method. The pore diameter was defined as the position of the maximum in the pore-size distribution.

2.4. Test of catalytic activity

The activities of these catalysts for CO oxidation were conducted in a temperature-programmed quartz tubular reactor (6 mm i.d.) under an ambient pressure. No pretreatment was applied before the catalytic test. The reactant gas mixture of 1.0 vol.% CO in air was allowed to pass through about 50 mg of catalyst at a total inlet flow rate of 100 mL min⁻¹, corresponding to a space velocity of 120,000 mL h⁻¹ g_{cat}⁻¹. The composition of effluent gas was monitored by an online gas chromatograph (SP-6890) equipped with a molecular sieve 13X column in conjunction with a thermal conductivity detector (TCD). Temperature during these tests was ramped at 3 °C min⁻¹. The catalytic data were collected under steady-state conditions. At each temperature point, three data points were collected and the final data point was obtained by averaging them.

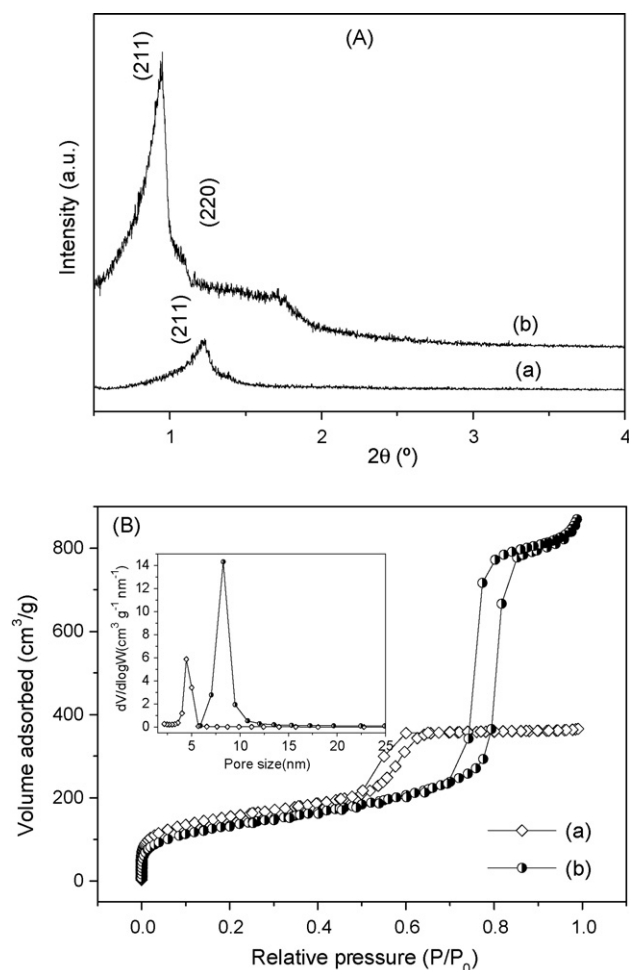


Fig. 1. (A) The small-angle XRD patterns of silica templates KIT-6-40 (a) and KIT-6-130 (b), (B) N_2 sorption isotherms of the mesoporous silica KIT-6-40 (a) and KIT-6-130 (b), and the inset is the pore-size distribution curves calculated from desorption branch by BJH method.

3. Results and discussion

3.1. Characterization of mesoporous silica templates

Fig. 1A presents the small-angle XRD patterns of two silica samples. Both of them indicate the $la3d$ cubic ordered mesostructures. Compared with KIT-6-40, KIT-6-130 has well-resolved diffraction peaks which shift to lower degrees with higher intensities. This indicates that higher hydrothermal temperature resulted in increased porous regularity and larger unit cell parameter. The unit cell parameter a_0 calculated from the (2 1 1) diffraction peaks are about 17.78 nm and 23.00 nm for KIT-6-40 and KIT-6-130, respectively. The nitrogen adsorption–desorption isotherms of the two silica samples are shown in Fig. 1B. Both of the samples exhibit type-IV isotherms with H1 hysteresis loops, characteristic of mesoporous silica with cylindrical pore geometry. Along with increasing aging temperature during the hydrothermal process, a shift of adsorption step and hysteresis loop toward higher relative pressure is observed, which indicates that pore size of the synthesized KIT-6 increases. Besides, the sharp capillary condensation over a narrow relative pressure region of both samples indicates that the pore-size distribution is relatively narrow (Fig. 1B inset). The textural parameters including BET specific surface area, pore-volume, and pore size of KIT-6-40 and KIT-6-130 determined by N_2 sorption data are given in Table 1. The average pore-wall thickness t_w of the KIT-6 template can be calculated from the small-angle X-ray diffraction

and adsorption data on the basis of the formula as follows [38]:

$$t_w = \frac{a_0}{2 - D_{\text{BJH}}}$$

where a_0 denotes the unit cell parameter and D_{BJH} represents the pore size. This equation is limited to the ordered mesoporous structure with cubic $la3d$ symmetry. The evaluated average pore-wall thickness of KIT-6-40 and KIT-6-130 is 4.41 nm and 3.22 nm, respectively (Table 1). As one can see from Table 1, along with increasing aging temperature, pore size and pore-volume of the synthesized KIT-6 increase while BET specific surface area and pore-wall thickness decrease, which are in consistent with the previous results [3].

3.2. Structure and crystallinity of the mesoporous Co_3O_4 replicas

The small-angle XRD patterns of the template-free mesoporous cobalt oxides are shown in Fig. 2A. A faithful replication of the cubic $la3d$ symmetry is only preserved for the Co_3O_4 nanocast from KIT-6 synthesized at 130°C . As is well-known, KIT-6 is composed of two sets of interpenetrating mesopores which are interconnected by micropores. According to the literatures [3,39], as in SBA-15, the fraction of micropores depends on the aging temperature. When the aging temperature is higher, there will be a larger fraction of micropores connecting the two mesopore systems. Correspondingly, the replica must grow across both sets of the mesopores in KIT-6. In contrast, when the aging temperature is lower, the micro-

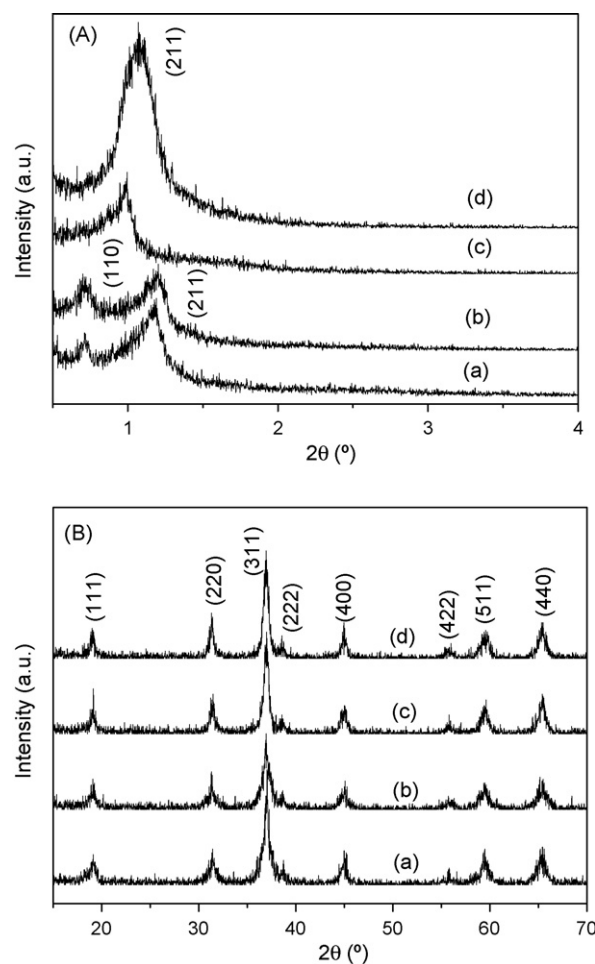


Fig. 2. Low-angle XRD patterns (A) and wide-angle XRD patterns (B) of ordered mesoporous Co_3O_4 replicas Co_3O_4 -300-KIT-6-40 (a), Co_3O_4 -500-KIT-6-40 (b), Co_3O_4 -300-KIT-6-130 (c) and Co_3O_4 -500-KIT-6-130 (d).

Table 1

Structural parameters of mesoporous KIT-6 silica templates.

Silica templates	a_0 ^a (nm)	S_{BET} ^b ($\text{m}^2 \text{g}^{-1}$)	V_t ^c ($\text{cm}^3 \text{g}^{-1}$)	D_{BJH} ^d (nm)	t_w ^e (nm)
KIT-6-40	17.78	526	0.56	4.48	4.41
KIT-6-130	23	468	1.32	8.28	3.22

^a a_0 , unit cell parameter.^b S_{BET} , BET surface area.^c V_t , pore-volume.^d D_{BJH} , average pore size.^e t_w , average pore-wall thickness.**Table 2**Physical properties and activity data of mesoporous Co_3O_4 spinel replicas.

Catalysts	d_{211} ^a (nm)	a_0 (nm)	S_{BET} ($\text{m}^2 \text{g}^{-1}$)	V_t ($\text{cm}^3 \text{g}^{-1}$)	D_{BJH} (nm)	t_w (nm)	T_{50} ($^\circ\text{C}$)
Co_3O_4 -300-KIT-6-40	7.48	18.33	105	0.23	5.26/10	–	68
Co_3O_4 -500-KIT-6-40	7.38	18.08	108	0.25	6.05/10.88	–	69
Co_3O_4 -300-KIT-6-130	9.03	22.12	69.1	0.12	3.89	7.17	95
Co_3O_4 -500-KIT-6-130	8.26	20.24	61.6	0.13	6.13	3.99	85

^a d -spacing calculated from (2 1 1) diffraction peak.

pores must be less developed, leading to less connectivity between two sets of pores. Correspondingly, the replica will grow within only one set of the KIT-6 mesopores. As shown in Fig. 2A, for Co_3O_4 -300-KIT-6-40 and Co_3O_4 -500-KIT-6-40, a new reflection indexed as (1 1 0) which is caused by the initial low interconnectivity of the parent silica is emerging in the low-angle range, resulting in a lower symmetry $I4_132$ [35,40]. As to Co_3O_4 -300-KIT-6-130 and Co_3O_4 -500-KIT-6-130, although they maintain the original $Ia3d$ symmetry of the template, the higher-order reflections are not very pronounced or well resolved, suggesting loss in structural order during the replication process. This may be owing to both the incomplete precursor pore filling of the silica template and relative large volume shrinkage during the thermal transformation from cobalt precursor to cobalt oxide. Moreover, the diffraction peaks of the sample calcined at higher temperature shift a little to higher two-theta angle, indicating a smaller cell parameter. The d_{211} values calculated from the (2 1 1) characteristic diffraction peaks and corresponding unit cell parameters (a_0) are listed in Table 2.

The wide-angle XRD patterns (Fig. 2B) of the cobalt oxide replicas show broadened and weak Bragg diffraction peaks, suggesting that these cobalt oxides are readily crystallized within the confined nanospaces. All the diffraction peaks of the four samples can be indexed to pure cubic phase of Co_3O_4 (JCPDS 65-3103). No impurity phase is detected. Besides, samples calcined at higher temperature of 500 $^\circ\text{C}$ show similar crystallinity with samples calcined at 300 $^\circ\text{C}$, which can be contributed to the confinement effect from the template's uniform mesopores.

3.3. FTIR analysis

FTIR analysis was conducted to determine the degree of silica matrix removal as well as the cobalt precursor decomposition. Fig. 3 shows the FTIR spectra of silica templates, $\text{Co}(\text{NO}_3)_2 \cdot 6\text{H}_2\text{O}$ and two representative Co_3O_4 replicas. As for KIT-6-40 and KIT-6-130, the absorption bands around 1080, 800 and 460 cm^{-1} may be assigned to Si–O–Si asymmetrical stretching vibration, symmetrical stretching vibration and bending vibration, respectively. The absorption band at around 960 cm^{-1} is originated from Si–OH stretching vibration. As for Co_3O_4 -300-KIT-6-40 and Co_3O_4 -300-KIT-6-130, two distinctive bands at around 668 (ν_1) and 571 cm^{-1} (ν_2), resulting from the stretching vibrations of the Co–O bond in Co_3O_4 , are present in the spectra. The ν_1 band is associated with Co^{2+} –O vibrations in a tetrahedral site, and ν_2 band is attributed to the Co^{3+} –O vibrations in an octahedral site [41,42]. For all the samples, the absorption bands at around 3420 and 1630 cm^{-1} are

related to the adsorbed H_2O molecules. By comparing the spectra of the two Co_3O_4 replicas with others, the absence of the characteristic absorption peaks belonging to the template or the cobalt precursor confirms that the silica template has been completely removed and the cobalt precursor has been completely transformed into Co_3O_4 .

3.4. TEM analysis of Co_3O_4 replicas

The four 3D mesoporous Co_3O_4 materials are examined by TEM (Fig. 4). All four samples show highly ordered pore structures. By examining many particles, it has been demonstrated that this highly ordered mesoporous structure is present throughout each material, confirming the high level of infiltration achieved by the solution precursor. Since the pore system in KIT-6 is three-dimensional in a cubic symmetry, almost spherical particles of the Co_3O_4 replica are normally developed. When KIT-6-40 is employed as the hard template, the TEM images of the corresponding Co_3O_4 replicas (a–d) show nanochannels along the view direction which is even more obvious at higher calcination temperature, implying that only one of the two sets of the channels of KIT-6 has been replicated. Consequently, uncoupled sub-frameworks are obtained. On the contrary, when KIT-6-130 is employed as the hard template, no nanochannels can be directly projected in the TEM images (e–h),

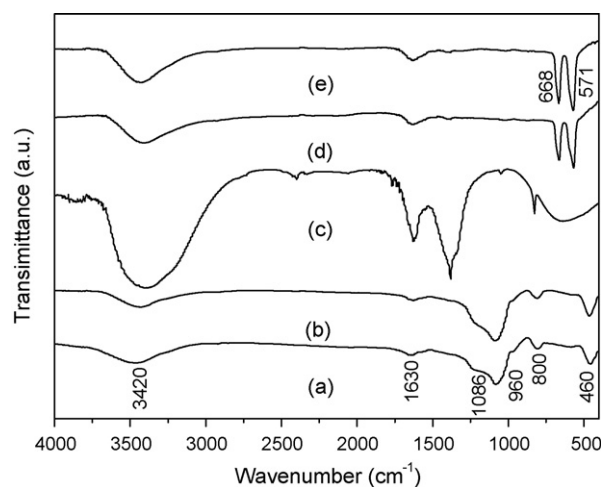


Fig. 3. FTIR spectra of the template KIT-6-40 (a) and KIT-6-130 (b), the precursor $\text{Co}(\text{NO}_3)_2 \cdot 6\text{H}_2\text{O}$ (c), the ordered mesoporous Co_3O_4 replicas Co_3O_4 -300-KIT-6-40 (d) and Co_3O_4 -300-KIT-6-130 (e).

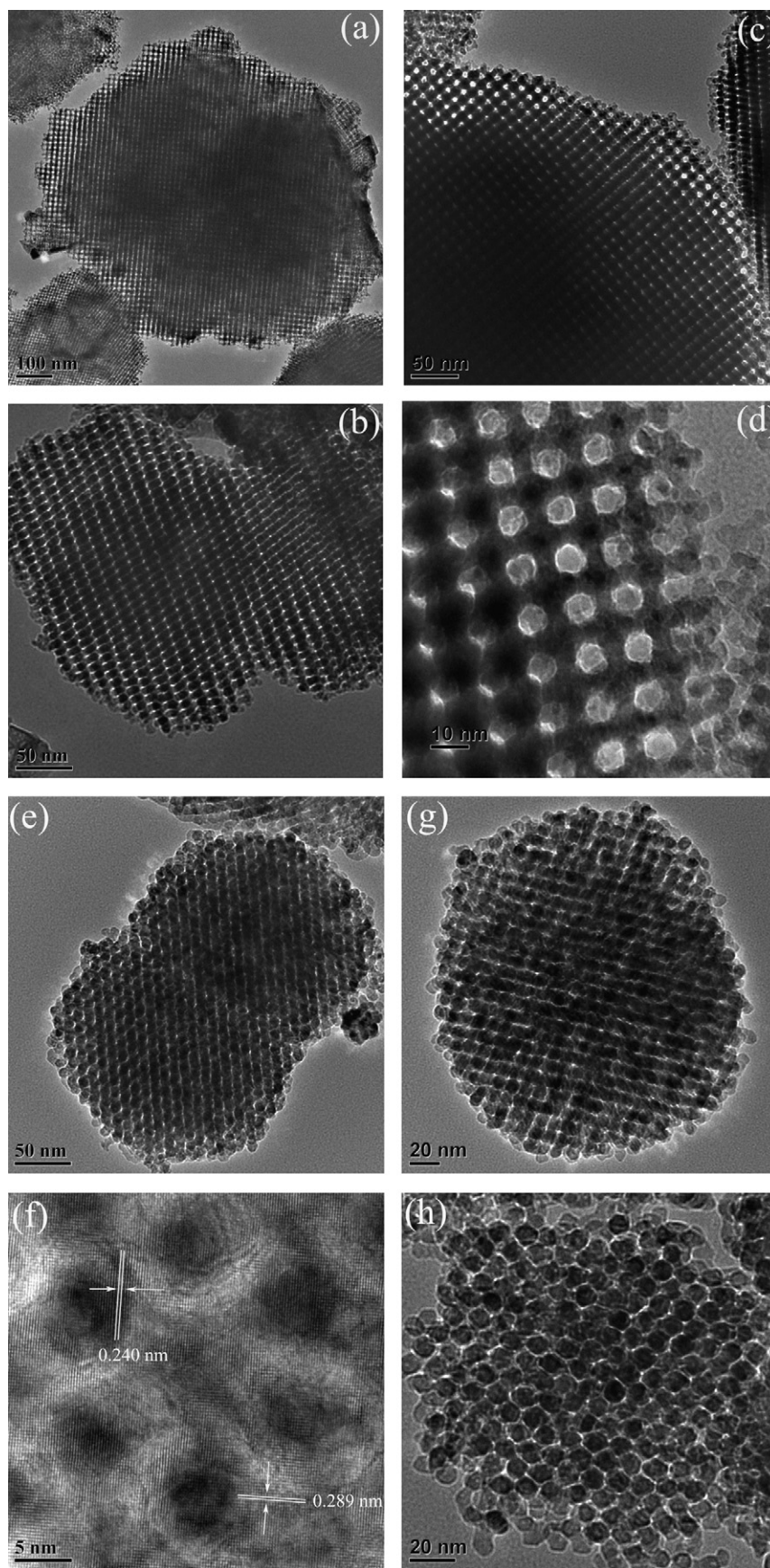


Fig. 4. TEM images of ordered mesoporous Co_3O_4 replicas: TEM images of Co_3O_4 -300-KIT-6-40 viewed along the $[100]$ and $[311]$ direction of the KIT-6-40 related cubic unit cell (a and b); TEM images of Co_3O_4 -500-KIT-6-40 viewed along the $[100]$ direction of the KIT-6-40 related cubic unit cell with different magnifications (c and d); TEM image of Co_3O_4 -300-KIT-6-130 viewed along the $[111]$ direction of the KIT-6-130 related cubic unit cell (e) and corresponding high-resolution TEM image on the $[\bar{1}12]$ zone axis of the Co_3O_4 unit cell (f); and TEM images of Co_3O_4 -500-KIT-6-130 viewed along the $[100]$ and $[111]$ direction of the KIT-6-130 related cubic unit cell (g and h).

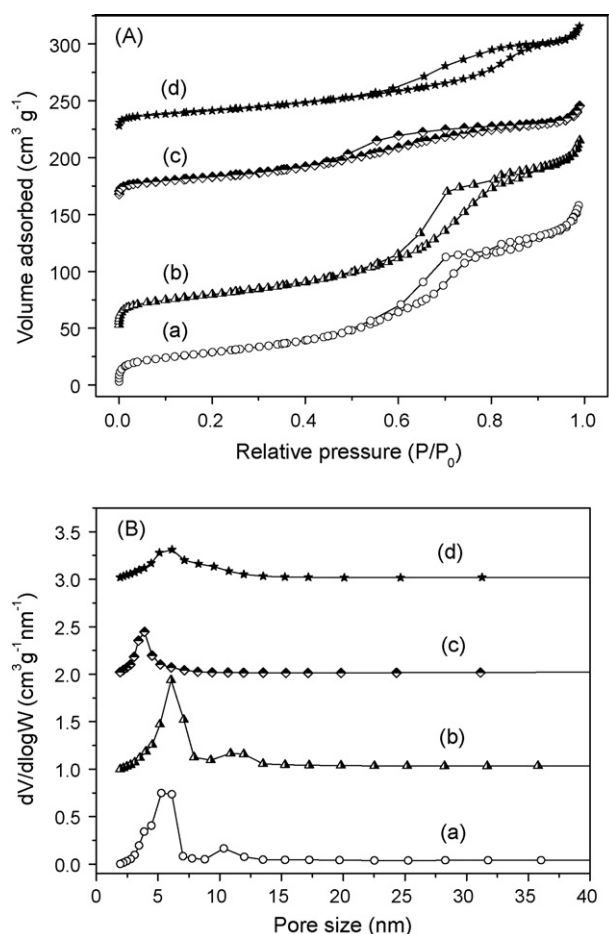


Fig. 5. (A) N_2 sorption isotherms and (B) pore-size distribution curves of ordered mesoporous cobalt oxide replicas Co_3O_4 -300-KIT-6-40 (a), Co_3O_4 -500-KIT-6-40 (b), Co_3O_4 -300-KIT-6-130 (c), and Co_3O_4 -500-KIT-6-130 (d).

indicating that the whole bi-continuous channel network in KIT-6 has been replicated. Consequently, coupled sub-frameworks are obtained [43]. Besides, lattice fringes can be discerned in the typical high-resolution TEM image of the Co_3O_4 -300-KIT-6-130 sample (Fig. 4f), confirming its crystalline characteristic. The two principal d -spacings measured from the image are 0.243 ± 0.01 nm and 0.285 ± 0.01 nm, corresponding to the (3 1 1) and (2 2 0) planes, respectively. The EDX measurement (not shown), performed on different domains of one of the template-free Co_3O_4 samples, reveals again almost the complete removal of silica template.

3.5. N_2 sorption analysis of Co_3O_4 replicas

Fig. 5 shows the N_2 adsorption–desorption isotherms and BJH pore-size distribution curves of the ordered mesostructured Co_3O_4 . The isotherm of the replica (Fig. 5A) shows a reduction in nitrogen uptake compared with the KIT-6 template. This is due to an increase in the density. The adsorption step at relative pressure (P/P_0) range of 0.4–0.9 is attributed to mesopores formed by dissolution of the silica template. The hysteresis loop reflects the capillary condensation phenomenon in the mesopores. The uptake at high pressure ($P/P_0 > 0.9$) is associated with the empty spaces between the particles. The adsorption step and hysteresis loop of Co_3O_4 -500-KIT-6-40 and Co_3O_4 -500-KIT-6-130 shifts to higher relative pressure relative to that of Co_3O_4 -300-KIT-6-40 and Co_3O_4 -300-KIT-6-130, respectively, which indicates that a higher calcination temperature may result in a larger pore size of the corresponding replica. The pore-size distributions of the meso-

porous Co_3O_4 replicas calculated from the desorption isotherms by the BJH method are shown as a plot of the relative pore filling versus pore size in Fig. 5B. It can be seen that Co_3O_4 -300-KIT-6-130 and Co_3O_4 -500-KIT-6-130 has unimodal pore-size distribution centered at 3.89 and 6.13 nm, respectively, which are larger than the pore-wall thickness of the silica template KIT-6-130. This can be attributed to the incomplete occupation of the pore space with Co_3O_4 . As indicated above, the pore size of Co_3O_4 -500-KIT-6-130 is larger than that of Co_3O_4 -300-KIT-6-130, which is the result of larger volume shrinkage at higher calcination temperature. In contrast to Co_3O_4 -300-KIT-6-130 and Co_3O_4 -500-KIT-6-130, Co_3O_4 -300-KIT-6-40 and Co_3O_4 -500-KIT-6-40 show different pore-size distributions with bimodal pore-size distributions. For Co_3O_4 -300-KIT-6-40 and Co_3O_4 -500-KIT-6-40, besides the peak centered at 5.26 and 6.05 nm, there is also a peak centered at 10 and 10.88 nm, respectively. The emergence of additional large pore is engendered from insufficient micropore connecting the channel-like enantiomeric systems, thus leading to an uncoupled sub-framework. This phenomenon is in fair agreement with the previous reports [3,35,39]. Theoretically, the relative large pore size of Co_3O_4 -300-KIT-6-40 and Co_3O_4 -500-KIT-6-40 is equivalent to the dimension of two walls plus a pore of KIT-6-40. Since calcination may result in shrinkage of the framework, the experimental pore size is a little lower than the theoretical pore size. The textural parameters including BET specific surface area, total pore-volume and pore diameter of mesoporous Co_3O_4 replicas are summarized in Table 2. When KIT-6-40 is employed as the template, the corresponding Co_3O_4 replicas have larger BET specific surface areas and pore-volumes. This may be correlated to the uncoupled sub-frameworks possessing rather loose structures as indicated by the TEM images above. The calculated pore-wall thicknesses of Co_3O_4 -300-KIT-6-130 and Co_3O_4 -500-KIT-6-130 using equation described above are also given in Table 2. Obviously, the pore-wall thicknesses are smaller than the pore size of the silica template KIT-6-130, which further corroborates the incomplete occupation of the pore space with Co_3O_4 .

3.6. Catalytic activity

The variation of the catalytic activity for CO oxidation as a function of the reaction temperature is investigated. Light-off temperature (T_{50}) as an index has been used to evaluate the activity of these spinel cobaltite replicas. The T_{50} of the CO oxidation obtained for these Co_3O_4 replica catalysts are listed in Table 2.

Fig. 6 presents the catalytic activities of mesoporous cobalt oxides before and after dissolution of the silica templates for CO oxidation when the calcination temperature of the precursor is fixed at 300 °C. A- Co_3O_4 -300-KIT-6-40 and A- Co_3O_4 -300-KIT-6-130 denote the as-synthesized Co_3O_4 /silica composites. On one hand, it is worthwhile to note that the catalytic activity for CO oxidation is greatly enhanced after dissolution of the silica template. The T_{50} decreases by 59 and 15 °C after dissolution of the silica template for Co_3O_4 -300-KIT-40 and Co_3O_4 -300-KIT-6-130, respectively. As demonstrated previously by Thomas and co-workers [44] for SBA-15 supported Co_3O_4 catalysts, there exists accessibility limitation of the CO and O_2 reactants to the active sites of the Co_3O_4 nanoparticles embedded in the SBA-15 porosity. Hence, we speculate the enhancement of the catalytic activity after dissolution of the silica template is ascribed to the unrestricted access of the reactant molecules to the Co_3O_4 particles in contrast with the as-synthesized Co_3O_4 /KIT-6 composites. On the other hand, Co_3O_4 -300-KIT-6-40 catalyst with T_{50} of 68 °C shows relatively higher activity compared with Co_3O_4 -300-KIT-6-130 catalyst with T_{50} of 95 °C. That is to say, the uncoupled frameworks with higher specific surface area and more open pore system possess a better performance for CO catalytic oxidation than the coupled frameworks. To

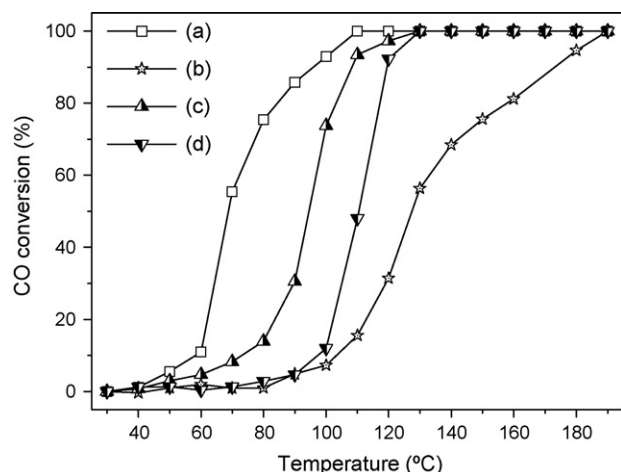


Fig. 6. Variation of the catalytic activities for CO oxidation as a function of the reaction temperature over samples before and after dissolution of the silica templates Co_3O_4 -300-KIT-6-40 (a), A- Co_3O_4 -300-KIT-6-40 (b), Co_3O_4 -300-KIT-6-130 (c) and A- Co_3O_4 -300-KIT-6-130 (d).

be worth mentioning, the catalytic stability is also evaluated over the best catalyst Co_3O_4 -300-KIT-6-40 (Fig. 7). The catalytic activity remains unchanged after three cycles and no loss of CO conversion is observed after 10 h on stream at 100 °C. Therefore, Co_3O_4 -300-KIT-6-40 catalyst exhibits both good cycling stability and excellent

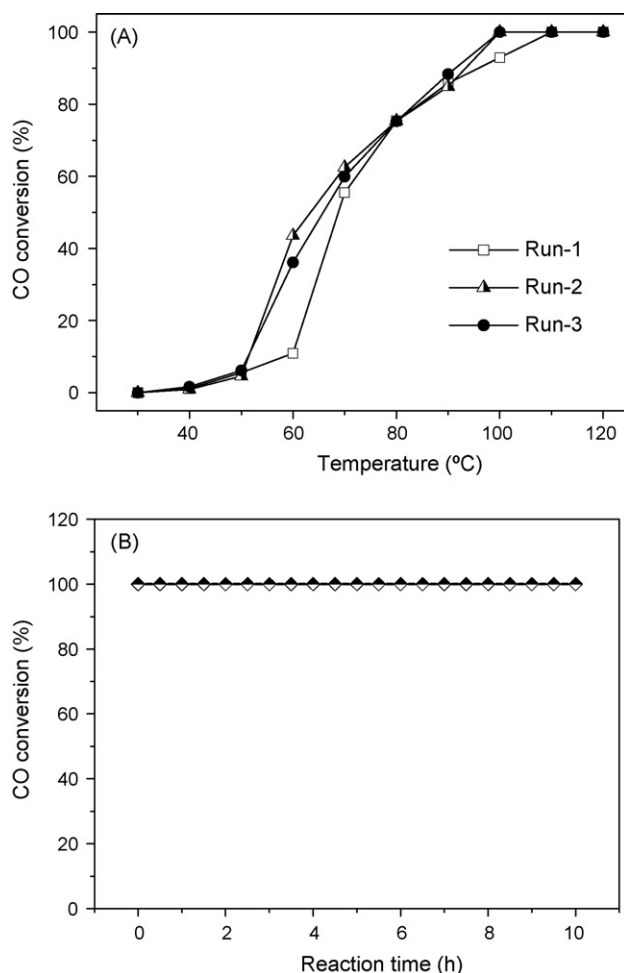


Fig. 7. Variation of the catalytic activities for CO oxidation as a function of the reaction temperature (A) and time (B) over the catalyst Co_3O_4 -300-KIT-6-40.

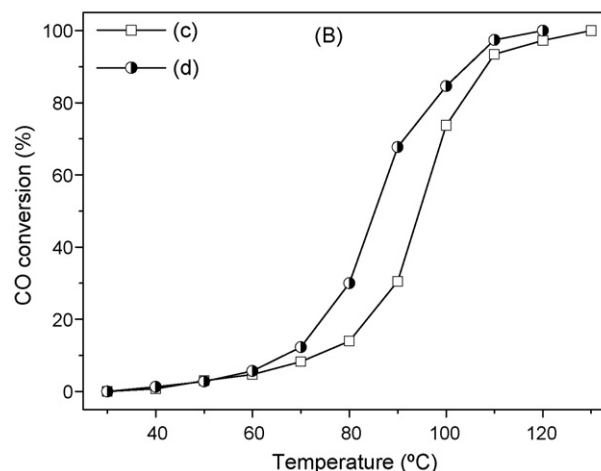
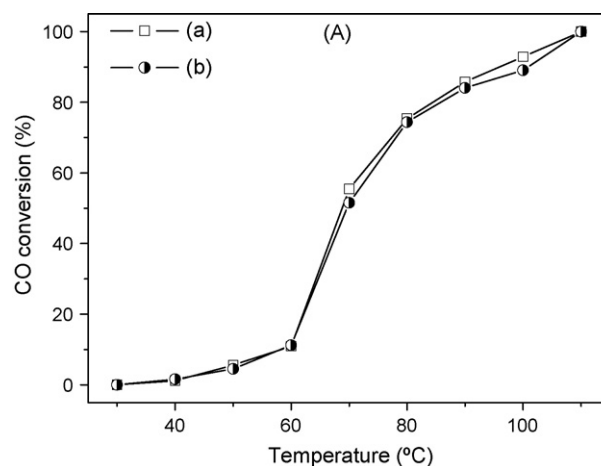


Fig. 8. Effect of calcination temperature on the catalytic activity for CO oxidation over ordered mesoporous Co_3O_4 replicas Co_3O_4 -300-KIT-6-40 (a), Co_3O_4 -500-KIT-6-40 (b), Co_3O_4 -300-KIT-6-130 (c) and Co_3O_4 -500-KIT-6-130 (d).

long-term stability, which may be contributed to the crystalline nature of the ordered mesoporous Co_3O_4 replica.

Fig. 8 illuminates the influence of calcination temperature of the precursor on the catalytic activity for CO oxidation. It is clear that when KIT-6-40 is employed as the hard template, calcination temperature has a negligible effect on the catalytic performance. This is because Co_3O_4 -300-KIT-6-40 and Co_3O_4 -500-KIT-6-40 have almost identical crystalline sizes and textural parameters as revealed by XRD and BET analyses above. However, when KIT-6-130 is employed as the hard template, the catalytic activity is slightly improved along with a higher calcination temperature. Although Co_3O_4 -300-KIT-6-130 and Co_3O_4 -500-KIT-6-130 show similar crystallinity, Co_3O_4 -500-KIT-6-130 has a much larger pore size relative to Co_3O_4 -300-KIT-6-130, which may be responsible for the slightly improved catalytic activity.

Furthermore, it is necessary to compare the catalytic data with those in the literatures to put our results in a proper perspective. Although the T_{50} value is a convenient index to compare the catalytic activity under the same experimental conditions, it is not particularly well suited to compare the catalytic activities of different catalysts under different test conditions (e.g., amount of catalyst, CO concentration, and flow rate). Instead, specific rate offers a better means of comparison [31]. As shown in Table 3, almost all the mesoporous Co_3O_4 catalysts prepared by the “bi-solvent” impregnation method (4.43 – $29.68 \text{ mmol g}^{-1} \text{ h}^{-1}$) here exhibit much faster specific rate than the mesoporous Co_3O_4

Table 3Comparison of published literature data for CO oxidation specific rates at 70 °C on Co₃O₄ catalyst with data obtained in this work.

Samples	Catalyst weight (mg)	CO concentration (%)	Flow rate (cm ³ min ⁻¹)	CO conversion (%)	Specific rate (mmol g ⁻¹ h ⁻¹)	References
Co ₃ O ₄ -300-KIT-6-40	50	1	100	55.41	29.68	This work
Co ₃ O ₄ -500-KIT-6-40	50	1	100	51.56	27.62	This work
Co ₃ O ₄ -300-KIT-6-130	50	1	100	8.27	4.43	This work
Co ₃ O ₄ -500-KIT-6-130	50	1	100	12.25	6.56	This work
Co ₃ O ₄ -135	200	1	60	22.5	1.81	[3]
Co ₃ O ₄ -100	200	1	60	95	7.63	[3]
PO-R230	500	4	20	11.07	4.29	[47]
Hollow Co ₃ O ₄ microspheres	100	1	200	0	0	[45]
Mesoporous Co ₃ O ₄ nanowires	107	2.7	30	2.61	20.28	[46]

prepared by the evaporation method (1.18–7.63 mmol g⁻¹ h⁻¹) reported in the literature [3]. A rough comparison of the mass-specific reaction rate with other forms of highly active Co₃O₄, such as hollow Co₃O₄ microspheres (0 mmol g⁻¹ h⁻¹) [45] and mesoporous Co₃O₄ nanowires (20.28 mmol g⁻¹ h⁻¹) [46], reveals the present catalysts show a comparable or even superior catalytic activity than the other Co₃O₄ catalysts reported so far.

4. Conclusion

A series of ordered mesoporous Co₃O₄ have been synthesized via nanocasting from the cubic *Ia3d* mesoporous KIT-6 silica. By varying the hydrothermal temperature, two kinds of Co₃O₄ replicas possessing coupled and uncoupled sub-frameworks were obtained. The uncoupled Co₃O₄ replicas show a lower symmetry *I4₁32* based on the small-angle XRD analyses with more open pore systems from the TEM images. These uncoupled Co₃O₄ replicas possess higher surface areas (105 or 108 m² g⁻¹), larger pore-volumes (0.23 or 0.25 cm³ g⁻¹) and bimodal pore-size distributions composed of small (5.26 or 6.05 nm) and large (10 or 10.88 nm) pores according to the nitrogen sorption test at 77 K. Excellent catalytic performances for CO oxidation over the uncoupled replicas were obtained with *T*₅₀ of 68 or 69 °C over Co₃O₄-300-KIT-6-40 or Co₃O₄-500-KIT-6-40. The CO catalytic activity was dependent on the textural parameters of the samples. A better performance could be achieved over the catalyst with higher surface area and more open pore system. The best catalyst Co₃O₄-300-KIT-6-40 also exhibited both good cycling stability and excellent long-term stability due to its crystalline nature, which maybe makes it an ideal support or catalyst for low temperature CO oxidation.

Acknowledgements

We thank the Chinese National Science Foundation (No. U0734002), Shanghai Basic Key Program (No. 09JC1415100) and Shanghai Nanotechnology Promotion Center (No. 0852nm0500) for the financial supports.

References

- [1] L.C. Wang, Q. Liu, X.S. Huang, Y.M. Liu, Y. Cao, K.N. Fan, Appl. Catal. B: Environ. 88 (2009) 204–212.
- [2] J.K. Zhu, Q. Gao, Z. Chen, Appl. Catal. B: Environ. 81 (2008) 236–243.
- [3] H. Tüysüz, M. Comotti, F. Schüth, Chem. Commun. 34 (2008) 4022–4024.
- [4] D. Gamarra, C. Belver, M.F. García, A.M. Arias, J. Am. Chem. Soc. 129 (2007) 12064–12065.
- [5] C.R. Jung, A. Kundu, S.W. Namb, H.I. Lee, Appl. Catal. B: Environ. 84 (2008) 426–432.
- [6] T.S. Mozer, D.A. Dziuba, C.T.P. Vieira, F.B. Passos, J. Power Sources 187 (2009) 209–215.
- [7] Q. Guo, Y. Liu, Appl. Catal. B: Environ. 82 (2008) 19–26.
- [8] J.L. Ayastuy, A. Gurbani, M.P. González-Marcos, M.A. Gutiérrez-Ortiz, Int. J. Hydrogen Energy. 35 (2010) 1232–1244.
- [9] M. Haruta, N. Yamada, T. Kobayashi, S. Iijima, J. Catal. 115 (1989) 301–309.
- [10] I.D. Gómez, I. Kocemba, J.M. Rynkowski, Appl. Catal. B: Environ. 88 (2009) 83–97.
- [11] X.S. Huang, H. Sun, L.C. Wang, Y.M. Liu, K.N. Fan, YongX.X. Cao, Appl. Catal. B: Environ. 90 (2009) 224–232.
- [12] Y. Denkwitz, M. Makosch, J. Geserick, U. Hörmann, S. Selve, U. Kaiser, N. Hüsing, R.J. Behm, Appl. Catal. B: Environ. 91 (2009) 470–480.
- [13] C.J. Jia, Y. Liu, H. Bongard, F. Schüth, J. Am. Chem. Soc. 132 (2010) 1520–1522.
- [14] M. Haruta, Chem. Rec. 3 (2003) 75–87.
- [15] M.S. Chen, D.W. Goodman, Catal. Today 111 (2006) 22–23.
- [16] S.M. Zhang, W.P. Huang, X.H. Qiu, B.Q. Li, X.C. Zheng, S.H. Wu, Catal. Lett. 80 (2002) 41–46.
- [17] M. Lundberg, B. Skårman, L.R. Wallenberg, Micropor. Mesopor. Mater. 69 (2004) 187–195.
- [18] G.G. Xia, Y.G. Yin, W.S. Willis, J.Y. Wang, S.L. Suib, J. Catal. 185 (1999) 91–105.
- [19] A.A. Mirzaei, H.R. Shaterian, R.W. Joyner, M. Stockenhuber, S.H. Taylor, G.J. Hutchings, Catal. Commun. 4 (2003) 17–20.
- [20] M. Krämer, T. Schmidt, K. Stöwe, W.F. Maier, Appl. Catal. A: Gen. 302 (2006) 257–263.
- [21] M. Li, D.H. Wang, X.C. Shi, Z.T. Zhang, T.X. Dong, Sep. Purif. Technol. 57 (2007) 147–151.
- [22] T. Cheng, Z.Y. Fang, Q.X. Hu, K.D. Han, X.Z. Yang, Y.J. Zhang, Catal. Commun. 8 (2007) 1167–1171.
- [23] J.L. Cao, Y. Wang, X.L. Yu, S.R. Wang, S.H. Wu, Z.Y. Yuan, Appl. Catal. B: Environ. 79 (2008) 26–34.
- [24] S.P. Wang, X.Y. Wang, J. Huang, S.M. Zhang, S.R. Wang, S.H. Wu, Catal. Commun. 8 (2007) 231–236.
- [25] J.L. Cao, Y. Wang, T.Y. Zhang, S.H. Wu, Z.Y. Yuan, Appl. Catal. B: Environ. 78 (2008) 120–128.
- [26] V. Iablokov, K. Frey, O. Geszti, N. Kruse, Catal. Lett. 134 (2010) 210–216.
- [27] Y. Hasegawa, K. Fukumoto, T. Ishima, H. Yamamoto, M. Sano, T. Miyake, Appl. Catal. B: Environ. 89 (2009) 420–424.
- [28] T.Y. Ma, Z.Y. Yuan, J.L. Cao, Eur. J. Inorg. Chem. 5 (2010) 716–724.
- [29] D.S. Zhang, C.S. Pan, L.Y. Shi, L. Huang, J.H. Fang, H.X. Fu, Micropor. Mesopor. Mater. 117 (2009) 193–200.
- [30] C.S. Pan, D.S. Zhang, L.Y. Shi, J.H. Fang, Eur. J. Inorg. Chem. 15 (2008) 2429–2436.
- [31] Y. Ren, Z. Ma, L.P. Qian, S. Dai, H.Y. He, P.G. Bruce, Catal. Lett. 131 (2009) 146–154.
- [32] W.H. Shen, X.P. Dong, Y.F. Zhu, H.R. Chen, J.L. Shi, Micropor. Mesopor. Mater. 85 (2005) 157–162.
- [33] J.K. Zhu, Q.M. Gao, Micropor. Mesopor. Mater. 124 (2009) 144–152.
- [34] L. Cui, J. Li, X.G. Zhang, J. Appl. Electrochem. 39 (2009) 1871–1876.
- [35] A. Rumpelcker, F. Kleitz, E.L. Salabas, F. Schüth, Chem. Mater. 19 (2007) 485–496.
- [36] F. Kleitz, S.H. Choi, R. Ryoo, Chem. Commun. (2003) 2136–2137.
- [37] M.I. Clerc, D. Bazin, M.D. Appay, P. Beaunier, A. Davidson, Chem. Mater. 16 (2004) 1813–1821.
- [38] T. Waitz, T. Wagner, T. Sauerwald, C.D. Kohl, M. Tiemann, Adv. Funct. Mater. 19 (2009) 653–661.
- [39] F. Jiao, A.H. Hill, A. Harrison, A. Berko, A.V. Chadwick, P.G. Bruce, J. Am. Chem. Soc. 130 (2008) 5262–5266.
- [40] T.W. Kim, F. Kleitz, B. Paul, R. Ryoo, J. Am. Chem. Soc. 127 (2005) 7601–7610.
- [41] Y.Z. Wang, Y.X. Zhao, C.G. Gao, D.S. Liu, Catal. Lett. 116 (2007) 136–142.
- [42] J. Ma, S.P. Zhang, W. Liu, Y. Zhao, J. Alloys Compd. 490 (2010) 647–651.
- [43] C. Dickinson, W.Z. Zhou, R.P. Hodgkins, Y.F. Shi, D.Y. Zhao, H.Y. He, Chem. Mater. 18 (2006) 3088–3095.
- [44] I. Lopes, A. Davidson, C. Thomas, Catal. Commun. 8 (2007) 2105–2109.
- [45] F. Teng, W.Q. Yao, Y.F. Zheng, Y.T. Ma, T.G. Xu, G.Z. Gao, S.H. Liang, Y. Teng, Y.F. Zhu, Talanta 76 (2008) 1058–1064.
- [46] Y.G. Zhang, Y.C. Chen, J.H. Zhou, T. Wang, Y.G. Zhao, Solid State Commun. 149 (2009) 585–588.
- [47] C.B. Wang, C.W. Tang, S.J. Gau, S.H. Chien, Catal. Lett. 101 (2005) 59–63.